



Tan, J. F., Gao, J. e., Barakos, G. N., Lin, C. L., Zhang, W. G. and Huang, M. Q. (2021)
Novel approach to helicopter brownout based on vortex and discrete element
methods. *Aerospace Science and Technology*, 116, 106839.

(doi: [10.1016/j.ast.2021.106839](https://doi.org/10.1016/j.ast.2021.106839))

This is the Author Accepted Manuscript.

There may be differences between this version and the published version. You are
advised to consult the publisher's version if you wish to cite from it.

<https://eprints.gla.ac.uk/242326/>

Deposited on: 21 May 2021

Novel approach to helicopter brownout based on vortex and discrete element methods

Jian Feng Tan^{a,*}, Jin er Gao^a, George N. Barakos^b, Chang Liang Lin^c, Wei Guo Zhang^d, Ming Qi Huang^d

^a*School of Mechanical and Power Engineering, Nanjing Tech University, Nanjing, P.R. China*

^b*CFD Laboratory, School of Engineering, University of Glasgow, Glasgow, UK*

^c*AVIC Harbin Aircraft Industry Group Corporation, Harbin, P.R. China*

^d*China Aerodynamics Research and Development Center, Mianyang, P.R. China*

Abstract

Numerical methods used for brownout were related to empirical and semi-empirical models, and particle-particle and particle-surface interactions were not included. A novel approach to helicopter brownout coupling a vortex method and a discrete element method is then developed. In this approach, the dynamics of individual sand particles, the particle-particle and particle-surface interactions are directly computed and coupled with flow field of helicopter in ground effect through the air forces. The approach is demonstrated for a scaled rotor of 172mm diameter in ground effect, as well as for the US Army EH-60L in brownout. The results show that the predicted radial velocity profiles and wall jet compare well with experiments and published CFD results, and the predicted behavior of brownout agrees with observations from flight tests of the EH-60L. Compared with Lagrangian dust cloud simulation, the predicted relative error of dust cloud is reduced by 57.09% in the taxi-pass case and 28.76% in the approach-to-touchdown case.

Keywords: helicopter brownout; particle-particle interaction; ground effect; vortex particle method; discrete element method

Nomenclature

b, f = edge lengths of a rectangular panel, m

A = area of a sand particle, m²

* Corresponding author.

E-mail address: Jianfengtan@njtech.edu.cn

C_D	= drag coefficient, non-dimensional
C_T	= thrust coefficient, non-dimensional
d_e	= equivalent diameter of a sand particle, m
e	= coefficient of restitution, non-dimensional
\mathbf{F}_c^n	= normal contact force between sand particles, N
\mathbf{F}_c	= contact force between sand particles, N
\mathbf{F}_f	= external force of a sand particle induced by flow field, N
\mathbf{F}_g	= body force of a sand particle, N
\mathbf{F}_s	= resultant force of a sand particle, N
G	= free-space Green's function, non-dimensional
G_h	= heat kernel function, non-dimensional
G^*	= equivalent shear modulus, Pa
I_s	= moment of inertial of a sand particle, $\text{kg}\cdot\text{m}^2$
K	= Biot-Savart kernel, non-dimensional
K_G	= gradient of the free-space Green's function, non-dimensional
m_s	= mass of a sand particle, kg
m^*	= equivalent mass, kg
\mathbf{n}	= unit normal vector, non-dimensional
N_{exp}	= number of experimental data, non-dimensional
\mathbf{r}	= position vector, m
R^*	= equivalent radius of a sand particle, m
Re	= Reynold number of a sand particle, non-dimensional
S_n	= normal stiffness, N/m
S_r	= rotor blade surface, m^2
S_{re}	= relative error, non-dimensional

S_{rw}	=	rotor wake surface, m^2
S_t	=	tangential stiffness, N/m
t	=	time, s
\mathbf{t}	=	tangential vector, non-dimensional
\mathbf{T}_s	=	result moment of a sand particle, N·m
\mathbf{u}	=	fluid velocity, m/s
\mathbf{v}_f	=	local fluid velocity of a sand particle, m/s
\mathbf{v}_h	=	ideal hover induced velocity, m/s
\mathbf{v}_s	=	resulting velocity of a sand particle, m/s
\mathbf{v}_n^{rel}	=	normal component of the relative velocity, m/s
\mathbf{v}_t^{rel}	=	relative tangential velocity, m/s
\mathbf{x}_i	=	position of a particle, m
y_i	=	predicted results, non-dimensional
y_{exp}	=	experimental results, non-dimensional
Y^*	=	equivalent Young's Modulus, Pa
\mathbf{a}_i	=	vector-valued vorticity of a particle, 1/s
β	=	normal stiffness, N/m
γ	=	bound circulation of vortex sheet, 1/s
δ_n	=	normal overlap, m
δ_t	=	tangential overlap, m
ε	=	smoothing radius, non-dimensional
η_ε	=	smooth distribution function, non-dimensional
μ	=	doublet of the rotor blade and wake surface, m^4/s
μ_s	=	coefficient of static friction, non-dimensional
μ_r	=	coefficient of rolling friction, non-dimensional

ν	=	kinematic viscosity, m^2/s
ν_1	=	Poisson's ratio of a sand particle, non-dimensional
ρ	=	air density, kg/m^3
σ	=	source of the rotor blade, m^3/s
τ_c	=	rolling friction, N
ϕ	=	velocity potential, m^2/s
ω	=	vorticity of flow field, $1/\text{s}$
ω_s	=	angular velocity of a sand particle, rad/s
ω_u	=	unit angular velocity vector, non-dimensional

1. Introduction

Helicopter brownout is an operational problem and a safety hazard. It reduces safety, leads to severe damage of engine components and rotor blades, and is reported as the main cause of several helicopter accidents. Brownout is generated by the entrainment of dust and ground debris due to the rotorcraft downwash and outwash during take-off and landing. Approximately three out of every four helicopter accidents reported during operations in Iraq and Afghanistan were caused by brownout, more than 20 helicopters and 50 lives since 2001 were related with brownout [1]. Furthermore, a degraded visual environment and almost half of the US forces rotorcraft airframe losses were due to brownout [2]. Therefore, the awareness of the impact of reduced visibility on safe rotorcraft operations in brownout conditions has been heightened, and improving safety during desert operations has recently received considerable attention.

Sensor systems [3], pilot cueing systems [4-6], and flight control solutions [7] enhancing situational awareness in brownout were developed. A semi-automatic system for hands-off landing in brownout conditions was also developed. Pilot training [8-10] and operational planning [11] were used to reduce the impact of brownout. However, the brownout rendering in training simulators was typically simplistic, lacking the level of fidelity required to properly characterize the formation and structure of the dust cloud. The flying tactics formed during training may not be unique and depend on the type of sediment and non-erodible surface elements on the ground. Brownout also differs considerably between different rotorcraft. Consequently, a more permanent solution to the brownout

problems may have to encompass design changes to the rotorcraft itself. Research suggests that optimization of the rotor and flight path can mitigate the effects of helicopter brownout [12-14]. To support those technologies and mitigate brownout effects, advanced numerical simulation tools, based on first principles, are required. Most of numerical methods used for brownout were related to empirical and semi-empirical models lacking the level of fidelity required to capture the complex interaction of the rotor downwash and debris transport. The brownout simulation ultimately entails the accurate prediction of the three-dimensional, unsteady flow field generated by a rotorcraft operating in ground effect (IGE), combined with accurate calculations of the trajectories and non-uniform concentrations of the sediment particles uplifted in the flow field. Furthermore, a multiphase fluid dynamics problem where the sediment and flow field are intrinsically coupled may also occur. This further contributes to the problem of brownout and drastically increases the complexity of understanding and modeling this phenomenon. Therefore, accurate predictions of the unsteady flow field in ground effect and the sand entrainment and transportation are two significant aspects in brownout simulation that remains a challenging modeling problem.

To date, numerical simulations of rotorcraft brownout have seen attention within the aeromechanics community and studies have already been undertaken through various simplifications and assumptions. A time averaged Navier-Stokes CFD analysis was developed to predict the rotor flow field and outwash for several rotorcraft configurations, and was used in brownout simulation of the U.S. Army [15]. However, a stochastic model of unsteady turbulent fluctuations was required to enable pick-up of the ground debris particles. A vorticity confinement and lifting line model, a simple momentum source model, a particulate convection model, and a simple entrainment model were coupled with an incompressible flow solver to predict the rotorcraft flow field in ground effect. Nevertheless, the dust cloud was treated as a continuous field instead of individual sand particles, and the complex saltation progress of sand particles was not taken into account [16]. Thus, A CFD solver based on Reynolds Averaged Navier-Stokes (RANS) equations and a momentum-source model was coupled with a particle entrainment and dispersion model to simulate brownout [17]. In this method, a convection-diffusion model was used to account for the transport of particles, and the entrainment from the bed into the flow was a function of the boundary condition and equilibrium mass flux. However, the ejection and ballistic impact of sand particles were not modelled. The time-accurate RANS-based CFD solver coupled with a Lagrangian sediment tracking algorithm developed by Leishman [18] was then used to analyze the evolution of brownout cloud [19]. Empirical models for the various phenomena involved in sediment transport, in which the entrainment of particles into the flow field was modelled by

a Bagnold-like model, and bombardment was represented by the model of Hu and Shao. However, the computational cost was larger, and contacts between particles were not taken into account. Thus, a hybrid free-vortex method and RANS solver coupled with the Lagrangian sediment tracking algorithm was developed to examine the capabilities of high-fidelity CFD analysis together with the sediment tracking algorithm to analyze the evolution of brownout clouds [20]. It was mainly used for hovering micro-rotors with few sand particles, and particle-particle and particle-surface interactions were not considered. More recently, a finite volume flow solver of German aerospace center with higher order schemes was coupled with the Lagrangian sediment tracking algorithm to simulate brownout through a one-way coupled post processing mode [21]. Results, nevertheless, were affected by the large computational requirements and excessive numerical dissipation in the wake. For brownout, numerical computations must compute the rotor wake dynamics over many rotor revolutions. Therefore, a fast, high fidelity brownout analysis tool has also been developed in the helicopter community.

A potential flow method [8-10, 23-25], such as free wake method, was developed to predict time averaged rotor wash and used in brownout analysis. A rotorcraft aerodynamic solver including a constant vorticity contour full-span free wake model, a vortex lattice lifting surface model, and a fast lifting surface source/doublet panel model was used to compute the rotor wash in ground effect and coupled with a debris transport model based on Lagrangian deposition and trajectory analysis, which is a U.S. Army suite of tools for simulating the effects of chemical/biological clouds, to simulate brownout [8]. This transport model focused on the pickup of the surface debris. Thus, a particle entrainment model including fluid threshold velocity, saltation, and flux rate of particles into the flow field was used and coupled with the particle transport model to simulate brownout. **The brownout module was also integrated into the U.S. Army's advanced prototyping engineering and experimentation laboratory rotorcraft flight simulations [9].** However, the viscous effects of the rotor wake and ground, and particle-particle interactions were not taken into account. The AgustaWestland 'Brownout Simulation Tool' was then developed by coupling a rotorcraft aerodynamic solver with a particle transport model [10]. In this tool, a full-unstructured panel method and a time-stepping full span free wake vortex model were used to compute aerodynamic load and flow field of a rotorcraft in the ground effect, while the entrainment of sand, dust and ground debris in the free air surrounding the rotorcraft was realized by tracking individual particles in a direct-way using Stokes-type drag laws coupled with inertia and threshold velocity of Bagnold. Nevertheless, the contacts between particles and ground were not accounted for. Additionally, the formation of the dust cloud in desert environments was modelled by

coupling the Brown's vorticity transport model and particle transport model through the particle flux, which represented the rate of entrainment of particle from the ground plane into the flow field [22]. But it needed empirical models to approximate the ground boundary layer, and did not simulate the uplift of the particles. Thus, a Lagrangian dust cloud simulation method was then proposed to understand the complicated two-phase flow of the rotorcraft brownout problems in recent years [18, 23, 24]. In this methodology, a free-vortex method and an inviscid image approach were used to simulate the flow field of the rotorcraft in ground effect, and a mesoscale three-dimensional sediment tracking method for low Reynolds number Stokes-type dust flows was developed to model dust cloud. The particle dynamics based on Basset-Boussinesq-Oseen equation, the entrainment from saltation and reingestion bombardment based on threshold velocity, threshold friction velocity [26], and model of Hu and Shao [27, 28] with assumptions were also used. Nevertheless, the processes of sediment trapping, uplift, saltation, bombardment were modelled based on assumptions since particle-particle and particle-surface interactions were not included.

Given the importance of the problem at hand, a novel approach to helicopter brownout coupling a vortex particle method and a discrete element method is proposed. The unsteady flow field is computed by a vortex-based method in which the aerodynamic loads of the blades are represented through an unsteady panel method. The behavior of the wake is captured by a viscous vortex particle method, and viscous effects on the ground are accounted for by a viscous boundary model. The dynamics of individual sand particles are calculated by a discrete element method where the particle-particle and particle-surface interactions are directly computed. The flow field of the rotorcraft is coupled with the dynamics of sand particles through the aerodynamic forces acting on individual sand particles. The method is demonstrated for a 172 mm-diameter scaled rotor in ground effect. The brownout of the US Army EH-60L in taxi-pass and approach-to-touch cases are also simulated and compared with experiments and published results of the Lagrangian dust cloud simulation.

2. Computational method

2.1. Aerodynamic model of helicopter in ground effect

Since brownout is mainly affected by the flow field and wake of a helicopter, the aerodynamic model of the helicopter in ground effect, including the unsteady rotor aerodynamic model, wake model, and viscous ground model, is firstly represented. Because the flow field, especially in the transition region where the flow runs from

vertical to horizontal, is dominated by the wake of the rotor blades [29-31], the helicopter has a distinct trailed wake with its own IGE characteristics. Thus, the aerodynamics and flow field of the helicopter in ground effect is modelled using the vortex-based solver [32], which has been applied to simulate the outwash and downwash of tandem rotors [30], flow fields of a tandem rotor affected by the ground and obstacles [33], flow field of multi-rotor configurations, including tandem and tilt rotors, during ship boarding [34]. In this solver, the velocity potential of the rotor is defined in a global reference frame as,

$$\phi(x, y, z, t) = \frac{1}{4\pi} \int_{S_i} \mu \mathbf{n} \cdot \nabla \left(\frac{1}{r} \right) dS - \frac{1}{4\pi} \int_{S_i} \sigma \left(\frac{1}{r} \right) dS + \frac{1}{4\pi} \int_{S_{rw}} \mu \mathbf{n} \cdot \nabla \left(\frac{1}{r} \right) dS \quad (1)$$

where σ and μ are the source and doublet distributions placed on the rotor blades (S_i) and on the wake surface (S_{rw}). \mathbf{n} denotes the outward unit normal vector of the surfaces, and \mathbf{r} is the position vector (x, y, z).

The Neumann boundary condition, the trailing-edge Kutta condition, the unsteady Bernoulli's equation are used to compute the velocity potential and unsteady airloads of the rotor. Furthermore, the Navier–Stokes equations in velocity-vorticity ($\mathbf{u}, \boldsymbol{\omega}$) in a Lagrangian frame are used to simulate the flow field and wake of the helicopter.

$$\frac{\partial \boldsymbol{\omega}}{\partial t} + \mathbf{u} \cdot \nabla \boldsymbol{\omega} = \nabla \mathbf{u} \cdot \boldsymbol{\omega} + \nu \nabla^2 \boldsymbol{\omega} \quad (2)$$

where ν is kinematic viscosity, $\boldsymbol{\omega} = \nabla \times \mathbf{u}$ is the vorticity field associated with the velocity field.

The Navier–Stokes equations are solved with the fourth-order Runge-Kutta scheme. The Biot-Savart law and symmetrical smoothing parameters are used to compute the velocity as:

$$\mathbf{u} = - \sum_{i=1}^N \frac{1}{\epsilon^3} K(\mathbf{x} - \mathbf{x}_i) \times \boldsymbol{\alpha}_i \quad (3)$$

where K is the Biot-Savart kernel for velocity evaluation, ϵ is the symmetrical smoothing parameters, \mathbf{x}_i and $\boldsymbol{\alpha}_i$ are the position and vector-valued vorticity of particle that are used to reconstruct the vorticity field as

$$\boldsymbol{\omega} = \sum_{i=1}^N \boldsymbol{\alpha}_i \eta_\epsilon(\mathbf{x} - \mathbf{x}_i), \text{ where } \eta_\epsilon(x) \text{ is a smooth distribution function.}$$

The particle strength exchange is used to consider the viscous diffusion effect, and a direct scheme is employed to account for the vortex stretching effect [35]. The operations count of this solver is reduced through the fast multipole method [36]. The vortices are shed from the blade surfaces via the applied Neumann boundary condition, and by converting the shed-wake doublet panels to vorticity [32], transported based on the Navier–Stokes equations. More details can be found in Ref. [32].

As the airloads, wake, flow field, and brownout of the helicopter can be affected by the ground, it is necessary to model its effects. A viscous boundary model based on a vorticity sheet is employed here [33, 34]. In this model, a Fredholm equation of the second kind that justifies the ground boundary condition is used and coupled with the aerodynamics of the rotorcraft through velocity induced by the vorticity as

$$\frac{\boldsymbol{\gamma} \times \mathbf{n}}{2} - \int_S K_G(\mathbf{x}_b - \mathbf{x}'_b) \times \boldsymbol{\gamma}(\mathbf{x}'_b) dS = \mathbf{u}(\mathbf{x}_b) + \nabla \phi \quad (4)$$

where $\boldsymbol{\gamma}$ is the bound vortex sheet, \mathbf{x}_b and \mathbf{x}'_b denote the positions of bound vortex sheets, and ϕ is the velocity potential on the bound vortex sheet induced by the helicopter, K_G is the gradient of the free-space Green's function G ,

$$K_G(\mathbf{x}_b, \mathbf{x}'_b) = \nabla G(\mathbf{x}_b, \mathbf{x}'_b) \quad (5)$$

The viscous boundary conditions are transformed to algebraic equations that provide the vector vortex sheet distribution. In a viscous flow, the presence of the ground and sand bed affects the flow by forcing the fluid to decelerate to zero velocity on the ground. The ground is then a source of vorticity and modelled as a vorticity flux. Thus, transfer of the vorticity of the vortex sheet to the nearby particles in the fluid domain is carried out. This is accomplished by solving a diffusion equation with the correct boundary conditions:

$$\begin{aligned} \frac{\partial \boldsymbol{\omega}}{\partial t} - \nu \Delta \boldsymbol{\omega} &= 0 \\ \boldsymbol{\omega}(t - \delta t) &= 0 \\ \nu \frac{\partial \boldsymbol{\omega}}{\partial n} &= \frac{-\boldsymbol{\gamma}(s)}{\delta t} \end{aligned} \quad (6)$$

The solution of the Eq. (6) can be computed in integral form using:

$$\boldsymbol{\omega} = \int_0^t \int_S G_h(\mathbf{x}, t, \mathbf{x}'_b, \tau) \boldsymbol{\gamma}(\boldsymbol{\xi}, \tau) dS d\tau \quad (7)$$

where $\boldsymbol{\xi}$ and τ are integrated surface and time, and G_h is the three-dimensional heat kernel, with $\tau < t$

$$G_h(\mathbf{x}, t, \mathbf{x}'_b, \tau) = (4\pi\nu(t-\tau))^{-1.5} \exp\left(-\frac{|\mathbf{x} - \mathbf{x}'_b|^2}{4\nu(t-\tau)}\right) \quad (8)$$

This flux must be emitted during a time Δt , and the vortex sheet $\boldsymbol{\gamma}$ must be distributed to neighbouring particles by discretizing Green's integral for the inhomogeneous Neumann problem corresponding to the diffusion equation. Then, a particle receives, from ground panel, an amount of "vorticity \times volume" given by:

$$\Delta \boldsymbol{\alpha}_i = \int_0^{\Delta t} \int_V \frac{d\boldsymbol{\omega}}{dt} dV dt \quad (9)$$

where V is the volume of the integration cuboid.

The rate of change of the vorticity, $d\boldsymbol{\omega}/dt$, due to the rectangular ground panel of uniform strength γ and size $b \times f$, is equal to

$$\frac{d\boldsymbol{\omega}}{dt} = \frac{\gamma}{2\Delta t \sqrt{4\pi vt}} \exp\left(-\frac{z^2}{4vt}\right) \left[\operatorname{erf}\left(\frac{(x-0.5b)}{\sqrt{4vt}}\right) - \operatorname{erf}\left(\frac{(x+0.5b)}{\sqrt{4vt}}\right) \right] \left[\operatorname{erf}\left(\frac{(y-0.5f)}{\sqrt{4vt}}\right) - \operatorname{erf}\left(\frac{(y+0.5f)}{\sqrt{4vt}}\right) \right] \quad (10)$$

where $\operatorname{erf}(x)$ is complementary error function.

After that, the vortex particles in the flow field can be tracked using the Navier–Stokes equations, and the flow field of brownout can be simulated; for more details, see Ref. [34].

2.2. Dynamics of individual sand particles

Brownout modelling is concerned with the movement of individual sand particles, which can be described as elements. The progress of brownout can be then depicted through a discrete element method (DEM) [37]. The DEM allows for fundamental studies of brownout, and no hypotheses on the rheological behaviour of the sand are needed. The DEM and its variants use Newton's second law to relate forces and moments within a system to spherical particle position and orientations as:

$$m_s \frac{d\mathbf{v}_s}{dt} = \mathbf{F}_s \quad (11)$$

$$I_s \frac{d\boldsymbol{\omega}_s}{dt} = \mathbf{T}_s \quad (12)$$

where m_s and I_s are the mass and moment of inertial of an individual sand particle, \mathbf{v}_s and $\boldsymbol{\omega}_s$ are the resulting translational and angular velocity of a sand particle, \mathbf{F}_s and \mathbf{T}_s are the resultant force and moment on a sand particle.

The DEM in macroscopic simulation considers forces and moments from a number of sources, internal and external, such as contact forces between sand particles \mathbf{F}_c , body forces \mathbf{F}_g , and external forces induced by flow field \mathbf{F}_f . These are added into the governing equations:

$$\mathbf{F}_s = \mathbf{F}_c + \mathbf{F}_f + \mathbf{F}_g \quad (13)$$

The DEM at larger spatial scales have generally been applied to granular solids whereby the contact forces are modelled using contact models which describe how two elements behave when they come into contact. The behavior of the individual elements affects the bulk behavior of the system. Here, the Hertz-Mindlin model [38, 39] is used in the integrated contact models. The contact force calculations are based on sphere overlaps, and the contact mechanics can be considered as a “spring-dashpot” configuration as shown in Fig. 1.

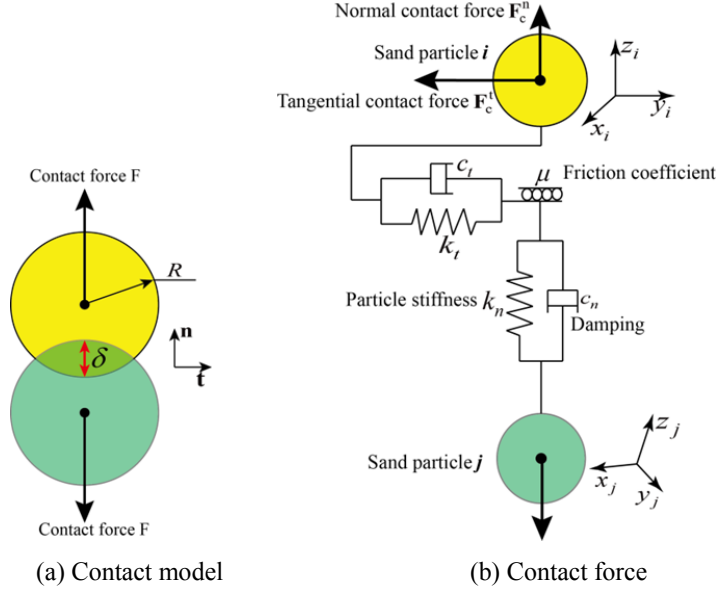


Fig. 1 Schematic of sand particle contact model

The normal contact force \mathbf{F}_c^n in the “spring-dashpot” configuration is given by:

$$\mathbf{F}_c^n = \frac{4}{3} Y^* \delta_n^{1.5} \sqrt{R^*} \mathbf{n} - 2\beta \sqrt{\frac{5S_n m^*}{6}} \mathbf{v}_n^{\text{rel}} \quad (14)$$

where Y^* is the equivalent Young’s Modulus, δ_n is the normal overlap, R^* is the equivalent radius, \mathbf{n} is the normal vector, m^* is the equivalent mass, $\mathbf{v}_n^{\text{rel}}$ is the normal component of the relative velocity, S_n and β are the normal stiffness. So

$$\frac{1}{R^*} = \frac{1}{R_1} + \frac{1}{R_2} \quad (15)$$

$$\frac{1}{Y^*} = \frac{1-v_1^2}{Y_1} + \frac{1-v_2^2}{Y_2} \quad (16)$$

where R_1 and R_2 are the radii of sand particles 1 and 2, Y_1 and Y_2 are the Young's Moduli of sand particles 1 and 2, ν_1 and ν_2 are the Poisson's ratios of sand particles 1 and 2.

Then, S_n and β are given by:

$$S_n = 2Y^* \sqrt{R^* \delta_n} \quad (17)$$

$$\beta = \frac{\ln e}{\sqrt{\ln^2 e + \pi^2}} \quad (18)$$

where e is the coefficient of restitution.

The tangential force is based on tangential overlap δ_t and the tangential contact force is given by:

$$\mathbf{F}_c^t = -S_t \delta_t \mathbf{t} - 2\beta \sqrt{\frac{5S_n m^*}{6}} \mathbf{v}_t^{\text{rel}} \quad (19)$$

where \mathbf{t} is the tangential vector, $\mathbf{v}_t^{\text{rel}}$ is the relative tangential velocity, S_t is the tangential stiffness written as:

$$S_t = 8G^* \sqrt{R^* \delta_n} \quad (20)$$

where G^* is the equivalent shear modulus written as:

$$\frac{1}{G^*} = \frac{1}{G_1} + \frac{1}{G_2} \quad (21)$$

The tangential force is limited by Coulomb friction $\mu_s \mathbf{F}_c^n$, where μ_s is the coefficient of static friction. The rolling friction is accounted for by applying a torque to the contacting surfaces as:

$$\boldsymbol{\tau}_c = -\mu_r F_c^n R \boldsymbol{\omega}_u \quad (22)$$

where μ_r is the coefficient of rolling friction, R is the distance of the contact point from the center of mass, $\boldsymbol{\omega}_u$ is the unit angular velocity vector.

The moment on a sand particle can be computed simply based on the contact forces, and the particle-surface interaction is similar to the particle-particle interaction where the surface is modelled as rigid solid and the equivalent Young's Modulus, equivalent shear modulus, and equivalent radius are equal to that of the particle.

2.3. Interaction between flow field and sand particles

Because the sizes of individual sand particles in the dust cloud are small and of the order of $100 \mu\text{m}$, the influence of the individual sand particles on the flow field is weak and neglected in this approach, while the influence of the flow field on the sand particles is taken into account. This is a one-way coupling approximation that holds well for low particle densities. Thus, the particle-fluid interaction is modelled **considering** the forces of the sand particles induced by the flow field, in the aerodynamic model of the rotorcraft. This can be written as:

$$\mathbf{F}_f = \frac{1}{2} \rho |\mathbf{v}_s - \mathbf{v}_f| (\mathbf{v}_s - \mathbf{v}_f) C_D A \quad (23)$$

where ρ and \mathbf{v}_f are the density and velocity of air, and A is the area of the sand particles.

Since spherical particles with an equivalent diameter of d_e are used, the area A is equal to $0.25\pi d_e^2$. The non-dimensional drag coefficient, C_D , can then be evaluated as an inverse function of the sand particles' Reynold number R_e , which is consistent with Stokes' results valid for a sphere moving through a viscous fluid, and the C_D is then written as:

$$C_D = \frac{24}{R_e} (1 + 0.15 R_e^{0.687}) \quad (24)$$

where

$$R_e = \frac{|\mathbf{v}_s - \mathbf{v}_f| d_e}{\nu} \quad (25)$$

For $R_e \ll 1$, the particles behave as in Stokes' flow, and C_D is given by

$$C_D = \frac{24}{R_e} \quad (26)$$

Coupling the particle-fluid interaction and the discrete element method with the aerodynamic model of rotorcraft in ground effect, enables brownout simulations.

2.4. Error analysis

The relative error of the dust cloud in brownout, RMS, is

$$s_{\text{re}} = \sqrt{\frac{1}{(N_{\text{exp}} - 1)} \left(\sum_{i=1}^{N_{\text{exp}}} (y_i - y_{i,\text{exp}})^2 \right)} \quad (27)$$

where N_{exp} , y_i , and y_{exp} are the number of experimental data, predicted results, and experimental data, respectively. A lower RMS indicates that the predicted results are in better agreement with experiments.

3. Numerical results and discussions

The test cases employed here, include the wake of a model rotor IGE, and the brownout of the EH-60L in taxi-pass and approach-to- touchdown cases. All these are based on well-defined experimental data available in the open literature. The axial and radial vortex locations of the rotor IGE are firstly predicted, and the radial velocity profile of a scaled rotor operating in ground effect is then computed. Finally, more complex cases with the brownout of the EH-60L are implemented to discuss the accuracy of the present approach.

3.1. Wake of the Lynx tail rotor in ground effect

The wakes of a rotor at distances above ground of $h/R=1.54$, $h/R=0.84$, and $h/R=0.52$ were simulated and compared with the experimental data of Light [40]. The rotor was made of four untwisted blades with constant chord as shown in Table 1. Its radius, airfoil, hover tip Mach number, chord Re at blade tip, chord, rotor solidity, and rotational speed were 1.105 m, NPL9615, 0.56, 2.3×10^6 , 0.18 m, 0.208, and 172.82 rad/s, respectively. The blade was modelled with 1200 panels composed of 60 panels in the chordwise direction, and 20 panels in the span-wise direction. The azimuthal angle step was 2.5° . The ground plane was modelled as $8 \text{ m} \times 8 \text{ m}$ with 1600 panels and was centred at the rotor axis.

Table 1 Main features of the tail rotor

Parameter	Value	Parameter	Value
number of blades	4	Re at blade tip	2.3×10^6
planform	rectangular	solidity	0.208
airfoil	NPL9615	tip Mach number	0.56
radius	1.105m	rotational speed	172.82 rad/s
chord	0.18m	twist	0°

The trajectories of the tip vortices of the rotor IGE are shown in Fig. 2. The axial and radial locations of the tip vortices are also shown and compared with the experiments and published CFD results [41]. The contraction of the tip vortices near the rotor plane and the expansion near the ground are captured well by the present method. The CFD had a tendency to over-estimate the wake expansion and axial convection, while a qualitative comparison with the present approach can be made indicating a satisfactory wake contraction, expansion, and axial convection.

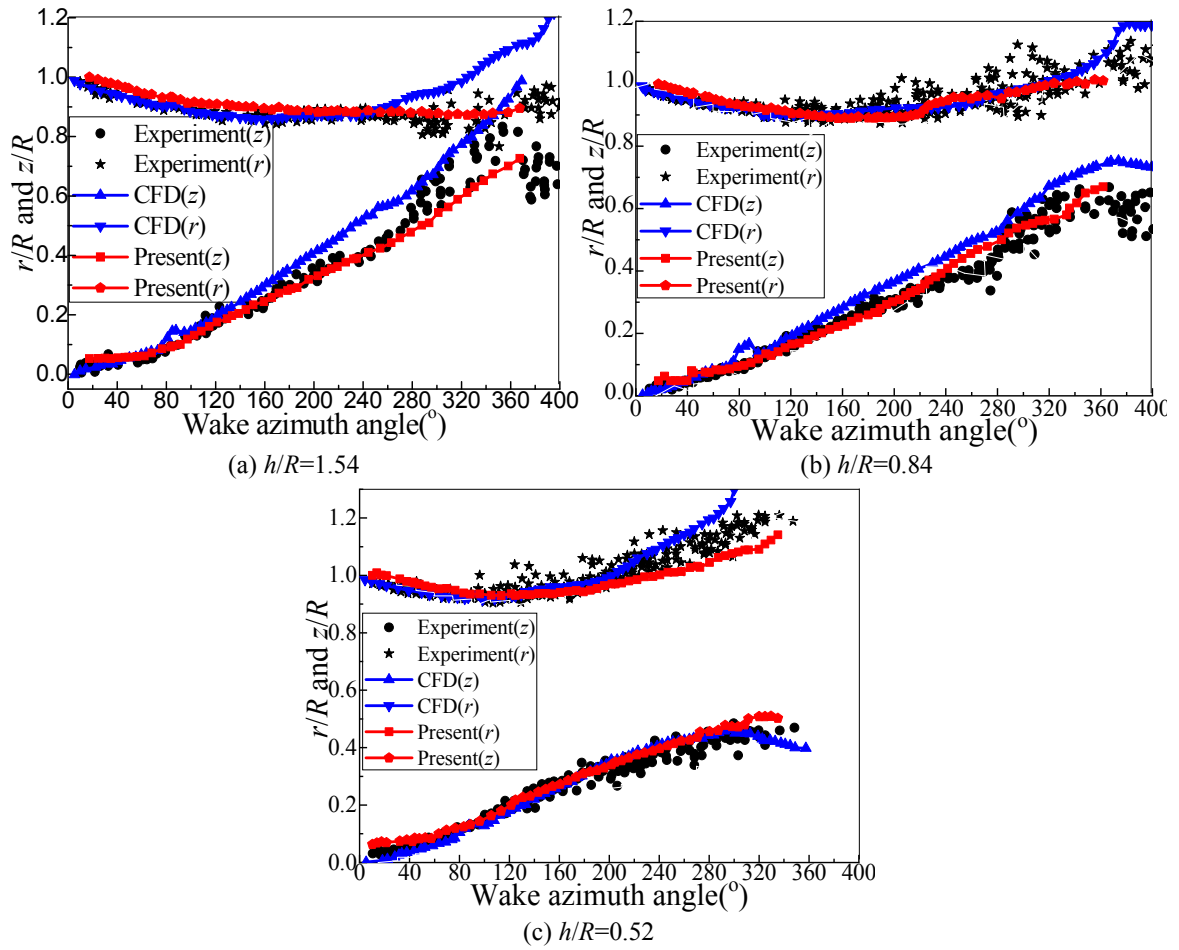
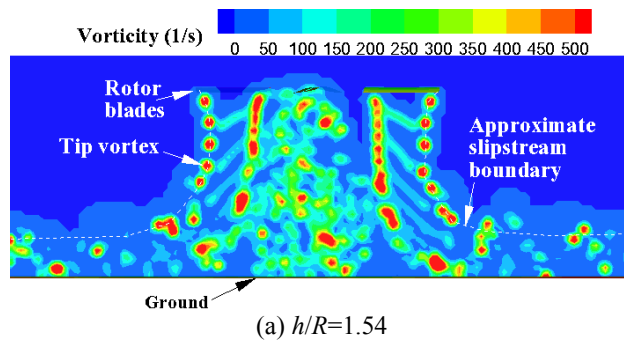


Fig. 2 Wake of the tail rotor in ground effect

The vorticity fields around the tail rotor IGE are plotted in Fig. 3. The tip vortices contract in the near wake, and expand in the far wake due to the effect of the ground plane. Additionally, unsteadiness in the far wake is also observed.



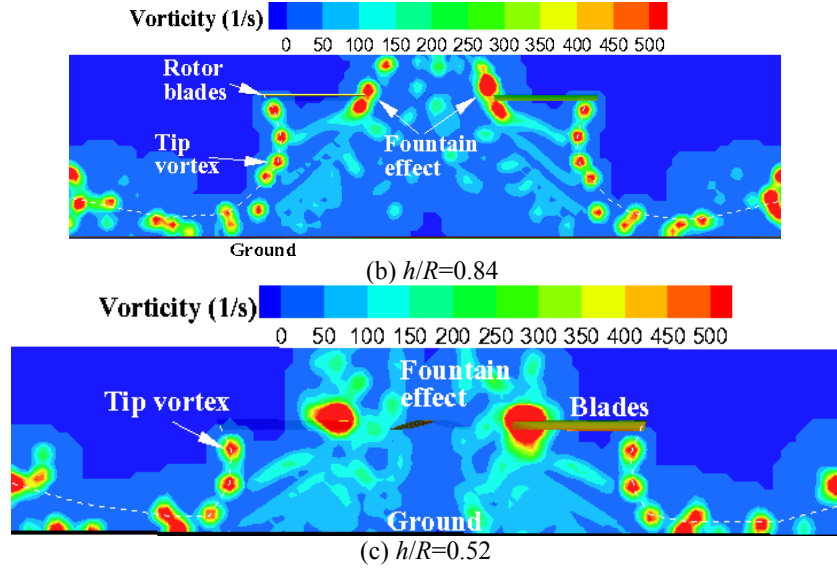


Fig. 3 Sectional vorticity of the tail rotor in ground effect

3.2. Wall jet of a scaled rotor in ground effect

The flow field around a rotor IGE was further compared with the experiments of Lee et al. [42]. The rotor was modelled with two untwisted rectangular blades of circular arc, cambered airfoil sections. The radius of the blade, chord, aspect ratio, and solidity were 86 mm, 19.6 mm, 4.39, and 0.14, respectively. The blades were set at a collective pitch of 12° , and the results were obtained at a tip Mach number of 0.08 as shown in Table 2. The blade was modelled with 1200 panels composed of 60 panels in the chordwise direction and 20 panels in the span-wise direction. The azimuthal step was 2.5° and the distance between the rotor and the ground plane was $1.5R$. The ground plane was a square plate $0.8\text{m}\times 0.8\text{m}$ and modelled using 1600 panels.

Table 2 Main features of the scaled rotor

Parameter	Value	Parameter	Value
number of blades	2	aspect ratio	4.39
planform	rectangular	solidity	0.14
airfoil	cambered	tip Mach number	0.08
radius	86mm	collective pitch	12°
chord	19.6mm		

The predicted rotor wake is shown in Fig. 4. The tip vortices contract radially after shed from the blades, and expand and stretch radially outward as they approach the ground surface. The onset of vortex pairing for the older vortices is also revealed in the Fig. 4. The vortices spin around each other, while the vortex sheets convect axially

faster than the blade tip vortices, and interact and merge with the older tip vortices as they age in the flow. Then, they produce a wall jet with a variety of eddies of various scales as the ground plane is approached.

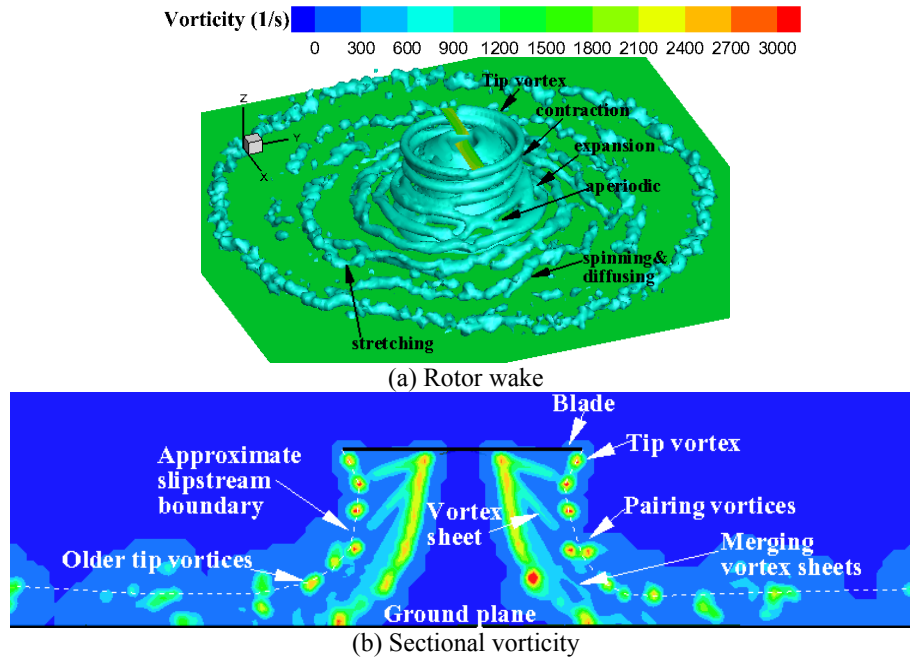


Fig. 4 Wake of the scaled rotor in ground effect

The time-averaged radial velocity at six radial distances, $r/R=0.8, 1.0, 1.25, 1.5, 1.75,$ and 2.0 , are predicted and compared with experimental data and published CFD results [43] in Fig. 5. The predicted time-averaged velocities have similar trends as the experiments and published CFD results. The estimated time-averaged velocities compare well with the CFD results at $r/R=0.8, 1.0,$ and 1.25 , whereas the present method and CFD under-predict the peak radial velocities. The peak radial velocities at $r/R=1.5$ and 1.75 were over-predicted by the CFD method, while they are under-predicted by the present method. Additionally, the peak radial velocity at $r/R=2.0$ was over-predicted by the CFD method, whereas the present prediction compares reasonably with experiments. Furthermore, the overall physics of the flow field is well captured. There are negative radial velocity excursions at and downstream of $r/R=1.5$ since the tip vortices are pushed outward as they approach the ground plane, while those tip vortices induce a negative radial velocity above the thickness of the wall jet. The rotor induced flow is forced to expand radially outward, creating the wall jet. The height of the wall jet is seen to decrease as one moves radially outward, which is similar to the experimental data. Therefore, the wake, radial velocity profiles, and wall jet of the rotor IGE are captured well by the present approach, which is foundation of the brownout simulation.

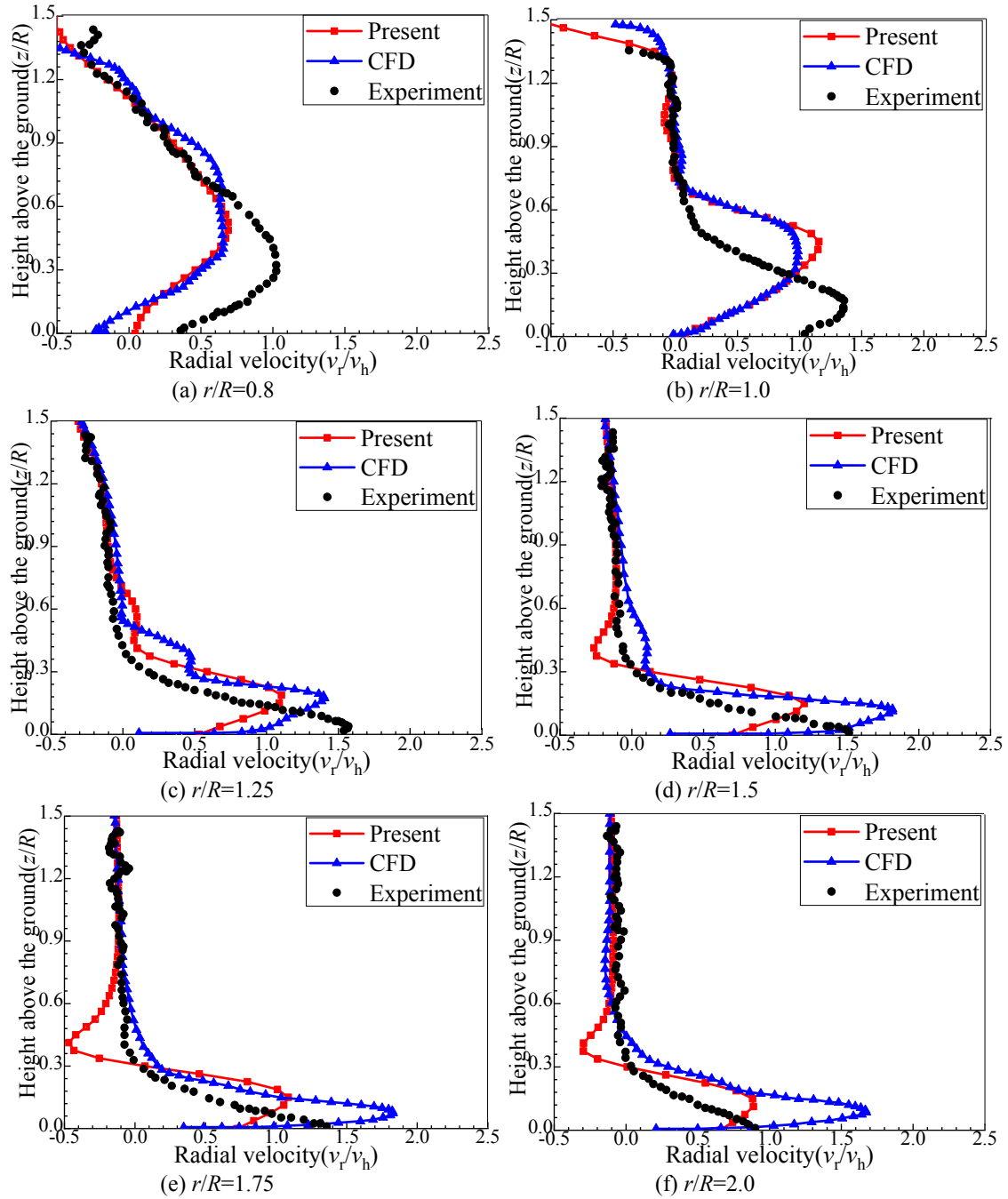


Fig. 5 Radial velocity of the scaled rotor in ground effect

3.3. Brownout of the EH-60L in taxi-pass case

The ability of the present approach to predict brownout of a helicopter in ground effect has been further investigated using the experiments of Wong and Tanner [44, 45]. The EH-60L was used to quantitative measurement of the evolution of the dust cloud generated by the helicopter operating under brownout condition. The

flight testing occurred at the Oasis Landing Zone (LZ), which was located at a remote section in the northern-most part of the US Army Yuma Proving Ground. The LZ consisted of seven lanes of varying widths, all running east to west. Lanes 1, 3, 5, and 7 were the ones through which the helicopter traveled as shown in Fig. 6. The sand at the LZ was extremely fine, similar to talcum powder, and was tilled by a tractor-pulled disc harrow. The tilled portion of the LZ was approximately 91.5 m long and 288 m wide. A photogrammetry setup using six 15.1 megapixel digital cameras was used to measure the shapes and external envelopes of brownout clouds. The behavior of brownout was simulated with the sizes of spherical sand particle between 1 and 100 μm based on the soil sample taken from the range. The taxi-pass case was performed at the EH-60L with a nominal forward airspeed of about 37 km/h and an altitude of 9.15 m. The trajectory of the helicopter at different times was shown and compared with the positions obtained using photogrammetry in Figs. 7 and 8. The simulation of brownout was taken for a duration of 10 s and the aerodynamic and brownout solution for this case was obtained by starting from $t=-2$ s.

The rotor of the EH-60L was modelled with four non-linear twisted rectangular blades of multi-airfoil sections. The radius of the blade, chord, sweep, and hover tip Mach number were 8.18 m, 0.5274 m, 20°, and 0.65, respectively. The blade was modelled with 1200 panels composed of 60 panels in the chordwise direction and 20 panels in the span-wise direction. The weight of the helicopter was set at 7394 kg, the azimuthal step was 5°, and the LZ was represented as a rectangle plate with 160 m \times 160 m dimensions and modelled using 10000 panels as shown in Fig. 8. The sand particles were randomly distributed in the rectangle plate with a total of 1×10^6 , and its radius was randomly between 1 and 100 μm . Its density, Young's Modulus, shear modulus, Poisson's ratio were 1000 kg/m³, 70000 Pa, 100000 Pa, and 0.25, respectively.

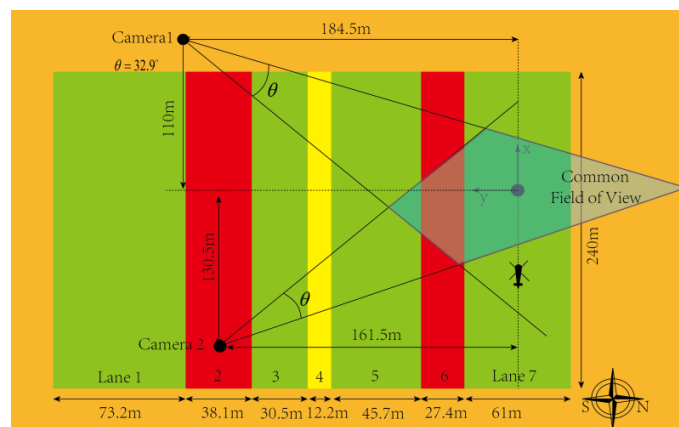


Fig. 6 Schematic of the Oasis LZ used for the brownout experiments in Ref. [44]

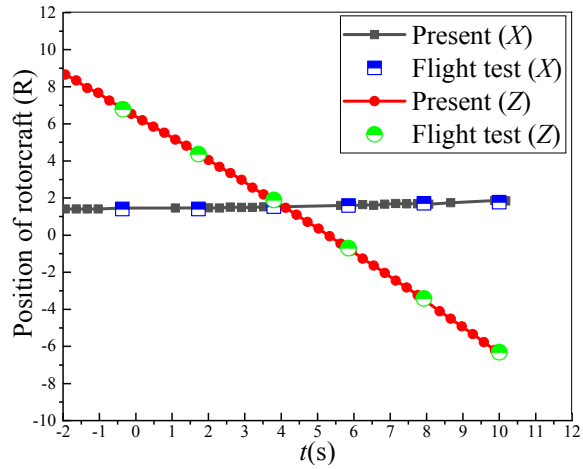


Fig. 7 Position of the helicopter

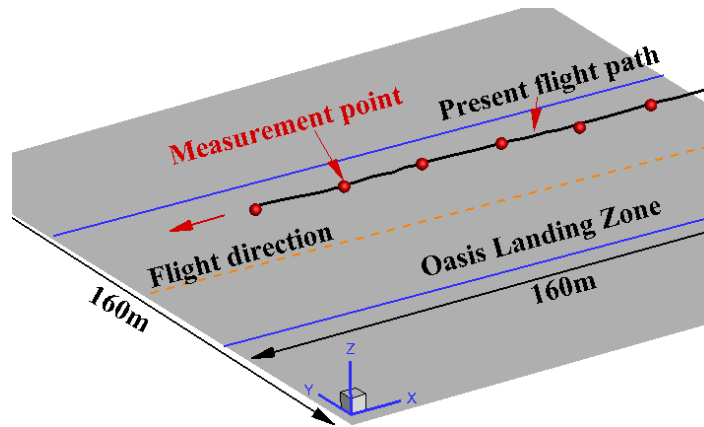


Fig. 8 Trajectory of the helicopter and model of the Oasis landing zone

The predicted dust clouds during the taxi-pass case are shown in Figs. 9-11. The flight test [44, 45] and results of the Lagrangian dust cloud simulation [23] are also plotted in Figs. 9-11 for comparison. The Lagrangian dust cloud simulation was composed by the models of the rotor flow in ground effect, sediment mobility, sediment tracing, and bombardment ejection based on a free-vortex method, an inviscid image approach, and a mesoscale three-dimensional sediment tracking method. The shapes of the evolving dust clouds along the longitudinal, lateral, and vertical directions at different times are consistent well with the measurements of the flight test. At the top views, the front edges of the dust clouds predicted by the presented approach and the Lagrangian dust cloud simulation are similar and slight smaller than that of the flight test at times of 0 s and 2 s. However, at $t=4$ s, the front edge of the dust cloud predicted by the Lagrangian dust cloud simulation is smaller than that of the flight test, while the present prediction compares well with the flight test. Moreover, the shape of the dust cloud predicted by the Lagrangian dust cloud simulation was contracted and slightly different from the flight test as shown in Fig. 11(a),

whereas the present predicted shape of the dust cloud is expanded along two sides as the flight test. Therefore, compared to the Lagrangian dust cloud simulation, the front edge and the shape of the dust cloud are predicted better.

At the side views, the shapes of the dust clouds predicted by the present method are similar to that of the Lagrangian dust cloud simulations and consistent with the flight tests at different times. The predicted location of the front edge of the dust cloud at time $t=0$ s is slightly smaller than that of the Lagrangian dust cloud simulation and the flight test. At time $t=2$ s, the location of the front edge predicted by the Lagrangian dust cloud simulation was slightly larger than that of the flight test. Conversely, the present prediction compares reasonably well with the flight test. Moreover, the discrepancy between the Lagrangian dust cloud simulation and flight test at time $t=4$ s is more obvious than that of time $t=2$ s, Nevertheless, the front of the dust cloud is captured reasonably well by the present approach. Furthermore, as the dust cloud moves backward, the height predicted by the Lagrangian dust cloud simulation firstly increases, and then decreases, indicating that the particles are lifted up at the position of the helicopter, and then descended to the ground behind it. However, the height of the dust cloud indicated by the flight test increases as the dust moves afterward. The height of the dust cloud is reasonably predicted by the present approach indicating that the particles are lifted up and suspended as the flight test. Therefore, the shape of the dust cloud is predicted better by the present approach than the Lagrangian dust cloud simulation.

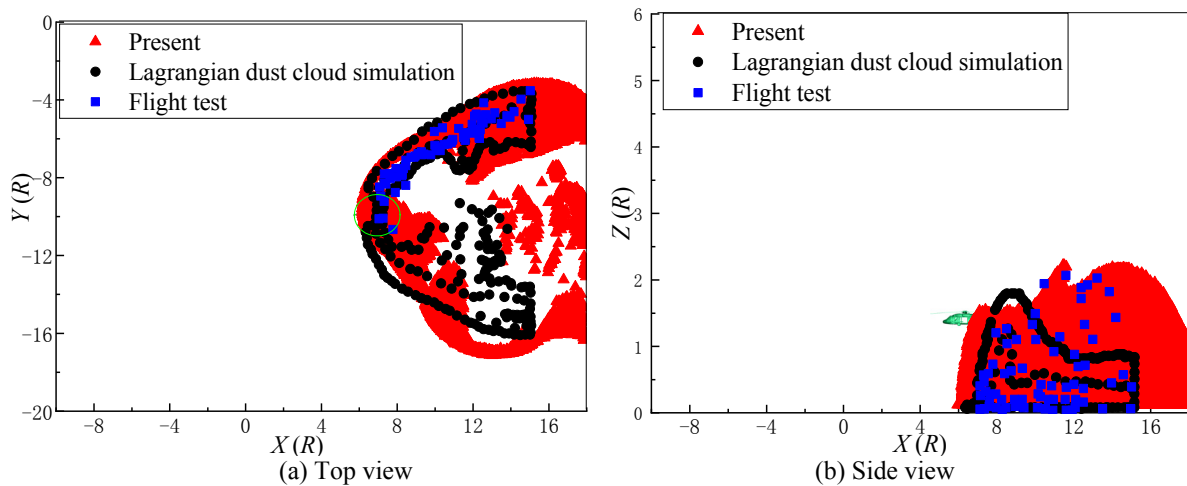


Fig. 9 Shape of the dust cloud at the $t=0$ s

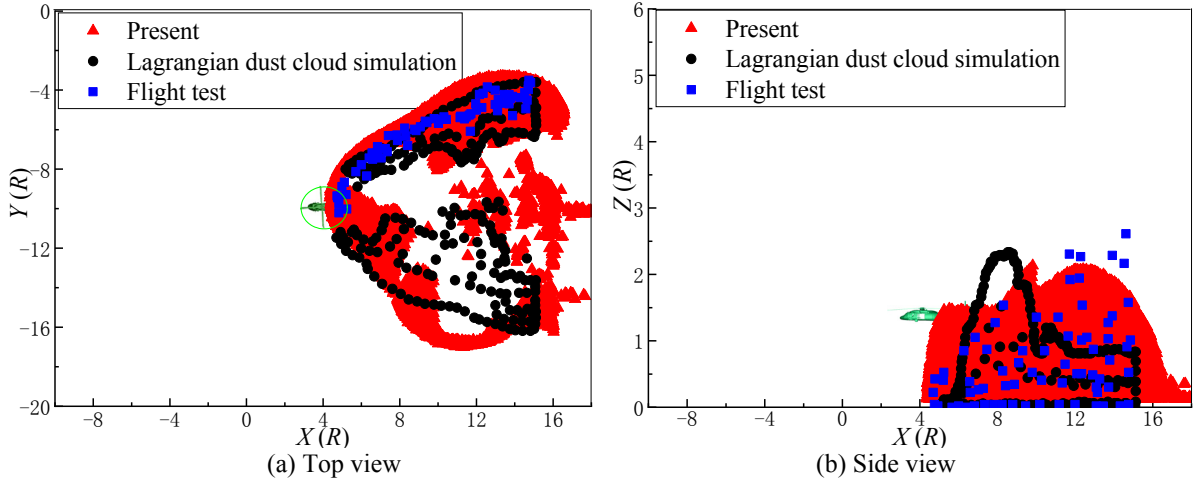


Fig. 10 Shape of the dust cloud at the $t=2$ s

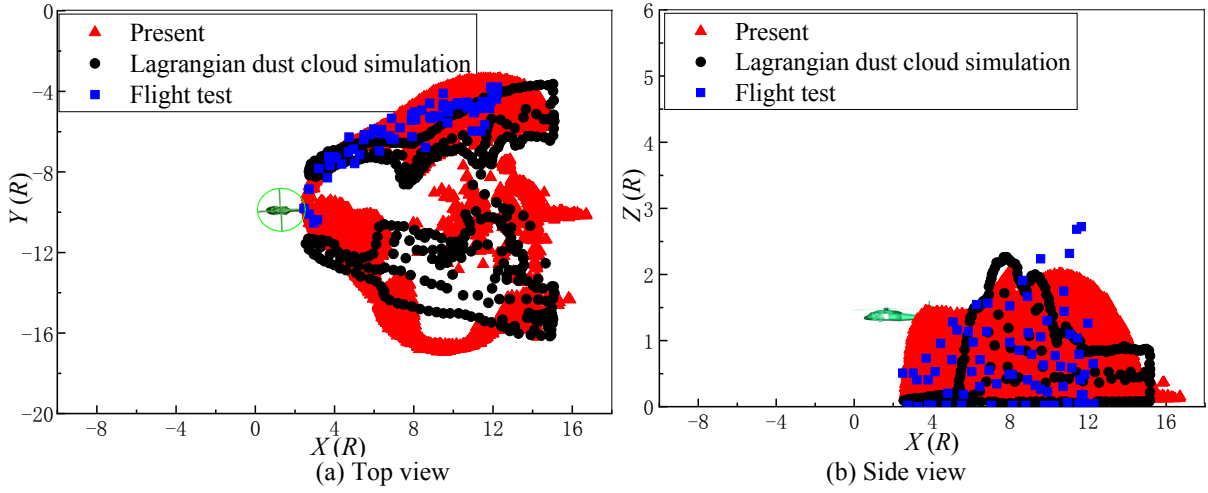


Fig. 11 Shape of the dust cloud at the $t=4$ s

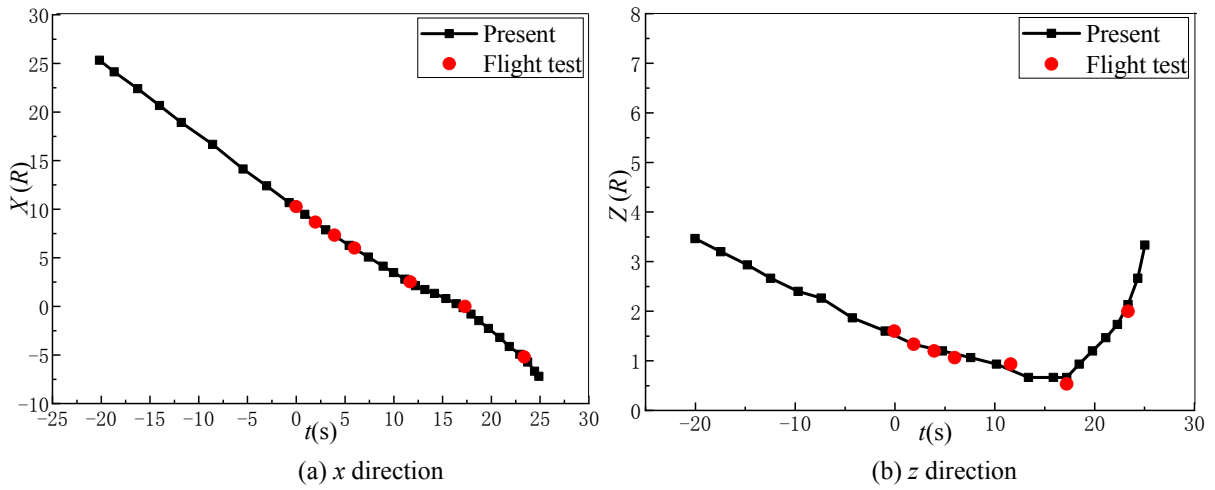
The RMSs between the predictions and the measurements are shown in Table 3. The present RMS of the top view at time $t=0$ s is slightly greater than that of the Lagrangian dust cloud simulation since the front edge of the dust cloud is over-predicted, while the present RMSs of the top view at other times are obviously smaller than that of the Lagrangian dust cloud simulation. This is because the shape of the dust cloud is predicted better, especially at time $t=4$ s as shown in Fig. 11(a). Furthermore, the present RMSs of the side view at different times are smaller than that of the Lagrangian dust cloud simulation since the front edge and height of the dust cloud are predicted reasonably well by the present approach. Compared with the top view, the predicted RMS of the side view is smaller since the shape of the dust cloud at the side view is captured better than that of the top view. The average RMS of the present method decreases by 57.09% compared with the Lagrangian dust cloud simulation. Therefore, the present approach can simulate the dust cloud with good accuracy.

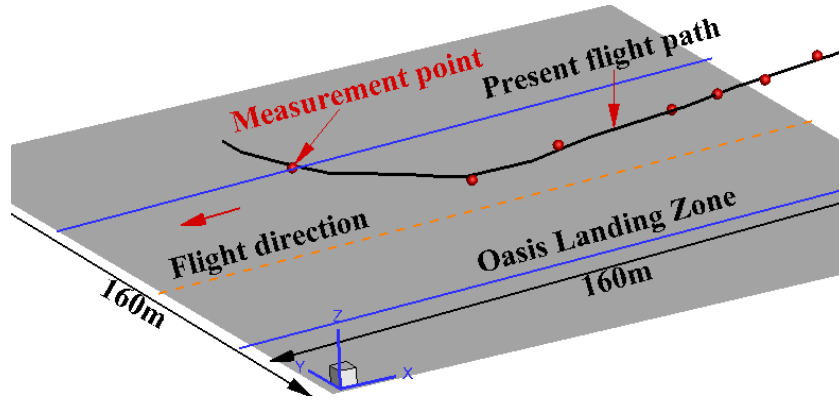
Table 3 RMSs of the predicted dust cloud at different times

Time (s)	Method	RMS of top view	Percentage (%)	RMS of side view	Percentage (%)
0	Lagrangian dust cloud simulation	0.2804	/	0.3736	/
	Present	0.3246	15.76	4.02E-2	-89.23
2	Lagrangian dust cloud simulation	0.5276	/	0.4973	/
	Present	0.2234	-57.66	0.1400	-71.84
4	Lagrangian dust cloud simulation	0.58702	/	0.4024	/
	Present	0.13235	-77.45	0.1523	-62.15

3.4. Brownout of the EH-60L in approach-to-touchdown case

The trajectory of the approach-to-touchdown case is also used to further validate the present approach. The position of the helicopter at different times during the approach-to-touchdown case is fitted and interpolated from the photogrammetric measurements and plotted in Fig. 12, and the flight speed can be calculated using finite differences. Note that there are small changes in the lateral position (y direction). Thus, it is not shown in Fig. 12. As the helicopter approaches the ground, it reaches an altitude of about 4.88 m and then climbs rapidly to fly out of the evolving dust cloud. Compared to the taxi-pass case, the approach-to-touchdown case is more complex.





(c) Trajectory of the helicopter

Fig. 12 Trajectory of the helicopter in the approach-to-landing case

The top and side views of the dust cloud in the approach-to-landing case at different times are provided in Figs. 13 to 18. The prediction of the Lagrangian dust cloud simulation and the flight test are also plotted. The shapes of the dust clouds at different times are predicted reasonably well with the flight test and the Lagrangian dust cloud simulation. At time $t=2$ s, the front edge of the dust cloud is under-predicted by the Lagrangian dust cloud simulation, while it is predicted well by the present approach and consisted with the flight test, see Fig. 13(a). The present predicted height of the dust cloud is similar to the result of the Lagrangian dust cloud simulation, and both results are higher than the flight test.

As the time increases to 4 s, the discrepancy between simulation and the flight test is strengthened due to the difference of the flow field near the ground plane as shown in Fig. 14(a). Compared to the previous time, the front edge of the dust cloud is slightly under-estimated by the Lagrangian dust cloud simulation, whereas it is over-estimated by the present approach. The height of the dust cloud is over-estimated by the present approach since the up-lifted velocities of the particles are slightly over-predicted.

At time $t=6$ s, the predicted shape of the dust cloud at the top view is similar to that of the Lagrangian dust cloud simulation, which shows similar trend as the flight test in Fig. 15(a). Nevertheless, the front edge of the dust cloud is under-predicted by both methods compared with the flight test. Furthermore, the height of the dust cloud predicted by the Lagrangian dust cloud simulation is obviously smaller than that of the flight test. As a contrast, the present prediction compares fairly well with the measurement as shown in Fig. 15(b).

The helicopter approaches its minimum altitude when the time t is 17 s, the comparison between the simulation and the flight test is now better as shown in Fig. 16. The simulated shape of the dust cloud is found to match well with the flight test, and the front edge of the dust cloud is slightly under-predicted by both the Lagrangian dust cloud

simulation and the present approach. Moreover, the height of the dust cloud is obviously under-estimated by the Lagrangian dust cloud simulation, whereas it is captured well by the present approach at the front part of the helicopter.

As the time increases to 23 s, the helicopter climbs, and the front edge of the dust cloud is slight under-predicted by the Lagrangian dust cloud simulation, while it is slightly over-predicted by the present approach shown in Fig. 17(a). In addition, the height of the dust cloud at the side view, shown in Fig. 17(b), is under-predicted by the Lagrangian dust cloud simulation. However, the present prediction compares reasonably well with the flight test.

Finally, as the time increase to 25 s, the helicopter climbs to the altitude of $3R$. The figure 18(a) shows that the front edge of the dust cloud is over-estimated by the Lagrangian dust cloud simulation, whereas it is predicted correctly by the present approach. Additionally, the comparison of the height of the dust cloud at the side view between the present approach and flight test is better than that of the Lagrangian dust cloud simulation.

As the helicopter approaches the ground plane, its wake moves to forward and both sides forming the ground vortex in the forward of the helicopter and rolled-up vortices in both sides of the helicopter. Thus, the dust cloud moves to forward and both sides in Figs. 14-16. As the time continued increases, the helicopter climbs after reaching its minimum of altitude, its wake moves to backward and insides resulting in decrease of the strength of the ground vortex in the forward of the helicopter and rolled-up vortices in both sides of the helicopter. Thus, the dust cloud moves to backward.

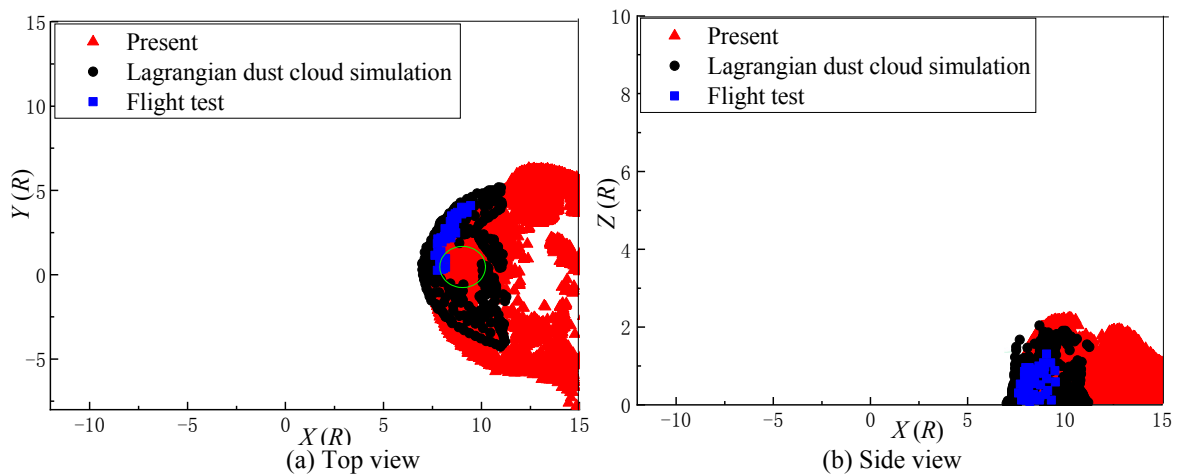


Fig. 13 Shape of the dust cloud at the $t=2$ s in approach-to-land case

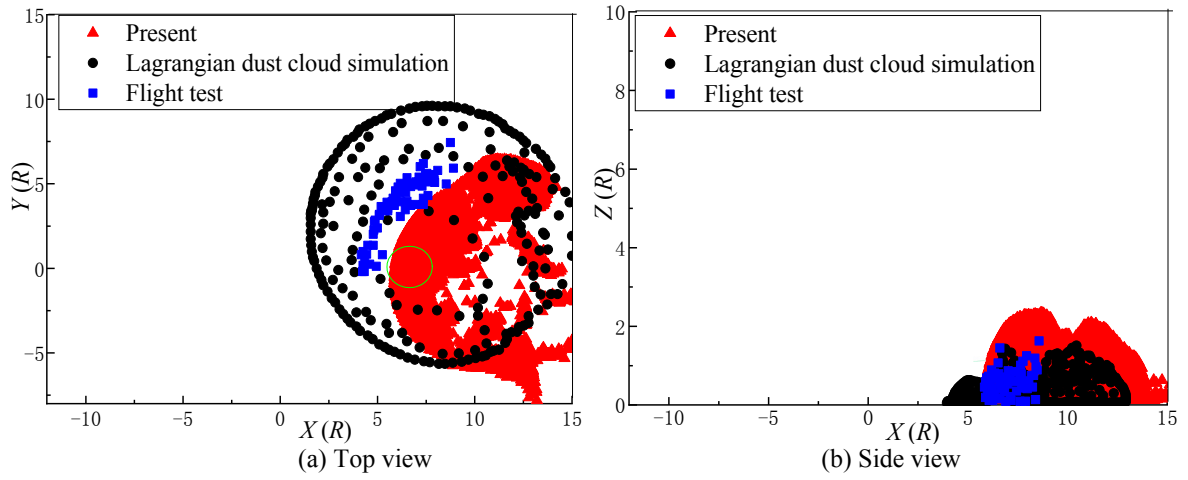


Fig. 14 Shape of the dust cloud at the $t=4$ s in approach-to-touchdown case

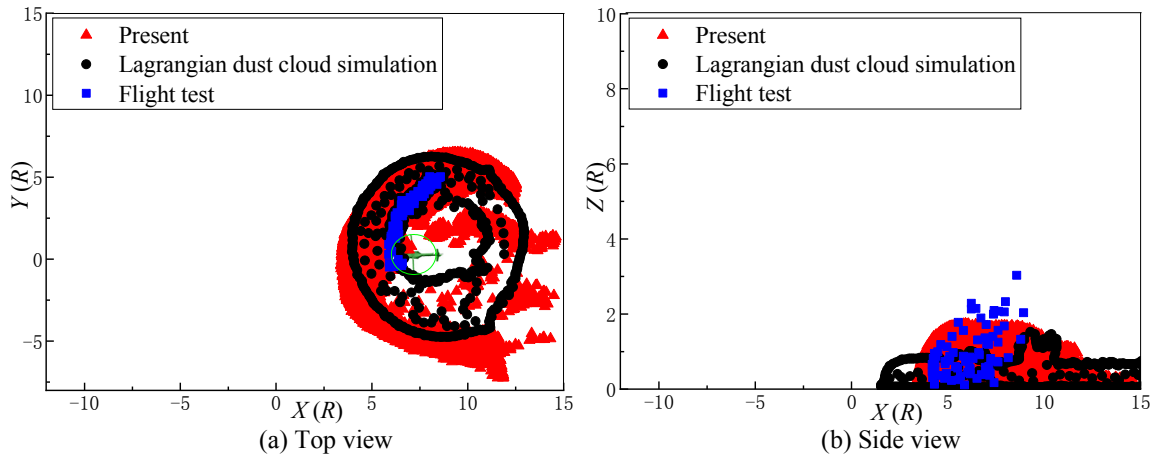


Fig. 15 Shape of the dust cloud at the $t=6$ s in approach-to-touchdown case

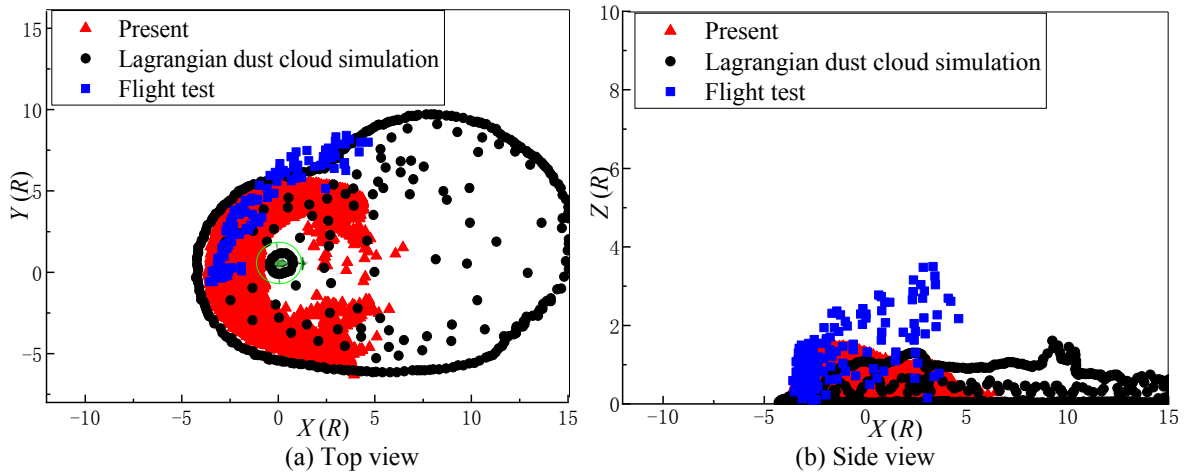


Fig. 16 Shape of the dust cloud at the $t=17$ s in approach-to-touchdown case

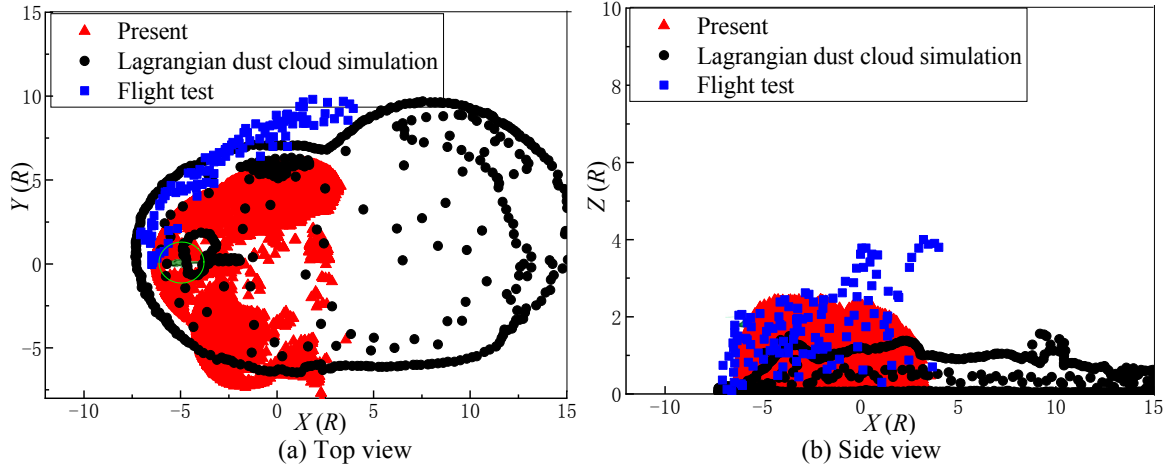


Fig. 17 Shape of the dust cloud at the $t=23$ s in approach-to-touchdown case

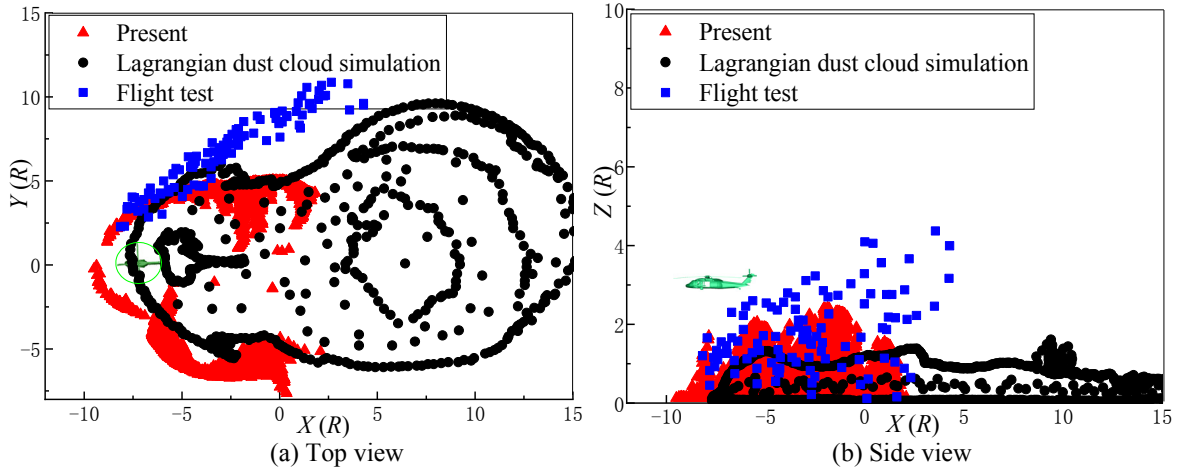


Fig. 18 Shape of the dust cloud at the $t=25$ s in approach-to-touchdown case

The RMSs between the predictions and the measurements in the approach-to-touchdown case are shown in Table 4. The present RMSs of the top view at time $t=2$ s, 6 s, 17 s, and 25 s are smaller than the Lagrangian dust cloud simulation since the front edges of the dust clouds are better predicted, while the present RMSs of the top view at time $t=4$ s and 23 s are larger than that of the Lagrangian dust cloud simulations. This is because the present method over-predicts the dust cloud, and the Lagrangian dust cloud simulations captured the front edge of the dust cloud at time $t=4$ s. The present model also over-predicts the size of the dust cloud at time $t=23$ s. Furthermore, the present RMSs of the side view at different times are obviously smaller than that of the Lagrangian dust cloud simulation since the front edge and height of the dust cloud are predicted reasonably well at the present approach. Compared with the top view, the predicted RMS of the side view is smaller because the shape of the dust cloud at the side view is captured better than that of the top view. The average RMS of the present method decreases by 28.76% compared

with the Lagrangian dust cloud simulation. Therefore, the present approach can simulate the dust cloud with good accuracy.

Table 4 RMSs of the predicted dust clouds at different times in approach-to-touchdown case

Time (s)	Method	RMS of top view	Percentage (%)	RMS of side view	Percentage (%)
2	Lagrangian dust cloud simulation	0.3438	/	0.203	/
	Present	0.2959	-13.912	0.2072E-2	-89.819
4	Lagrangian dust cloud simulation	1.0755	/	0.245	/
	Present	1.45572	35.344	2.316E-02	-90.573
6	Lagrangian dust cloud simulation	0.2375	/	0.5621	/
	Present	0.15578	-34.433	0.227	-59.539
17	Lagrangian dust cloud simulation	0.6081	/	0.944	/
	Present	0.1349	-77.798	0.8105	-14.186
23	Lagrangian dust cloud simulation	0.4907	/	1.1688	/
	Present	0.9259	88.670	0.7068	-39.523
25	Lagrangian dust cloud simulation	0.6722	/	1.1513	/
	Present	0.4717	-29.826	0.9264	-19.538

4. Conclusion

A novel approach to helicopter brownout is developed by coupling a vortex particle method and a discrete element method. The dynamics of individual sand particles including the particle-particle and particle-surface interactions is directly computed, and coupled with the flow field of the rotorcraft through the air forces acting on individual sand particles. The approach is applied to a scaled rotor in ground effect, as well as for the US Army EH-60L in brownout, and some conclusions can be drawn as follows:

- (1) The predicted trajectories of the tip vortices and the radial velocity profiles compare well with experimental data and published CFD results based on RANS equations. The contraction, expansion, merger of the tip vortices approaching to the ground are captured well, and the variations of the velocity and wall-jet near the ground are also captured.
- (2) The dust clouds of the EH-60L in taxi-pass and approach-to-touchdown cases are predicted reasonably well, and the behavior of the dust cloud of the EH-60L in both cases is well-captured.

- (3) Compared with the Lagrangian dust cloud simulation, the front edge of the dust cloud is predicted better by the present approach, and the height of the dust cloud predicted by the present approach is found to be more accurate.
- (4) Compared with the Lagrangian dust cloud simulation, the present predicted RMSs of the clouds are reduced by 57.09% in the taxi-pass case and 28.76% in the approach-to-touchdown case.

Declaration of competing interest

The authors declare that they have no known competing financial interests or personal relationships that could have appeared to influence the work reported in this paper.

Acknowledgments

This work was supported by the National Science Key Laboratory Foundation (Grant No. 6142220180202), Rotor Aerodynamics Key Laboratory Foundation (Grant No. RAL20200302), and National Natural Science Foundation of China (Grant No. 11502105).

References

- [1] L. Anderson, P. Doty, M. Griego, K. Timko, B. Hermann, J. Colombi, Solutions analysis for helicopter brownout, 9th Annual NDIA Systems Engineering Conference, 23-26 October, San Diego, CA, 2006.
- [2] Acquisition and Technology Programs Task Force, Department of defense aviation safety technologies report, Washington, DC: Defense Safety Oversight Council, Office of the Under Secretary of Defense for Personnel and Readiness, 2009, pp. 22-23.
- [3] C. Jansen, A. Wennemers, E. Groen, FlyTact: A tactile display improves a helicopter pilots landing performance in degraded visual environments, *Haptics: Perception, Devices and Scenarios*, 50 (24) (2008) 867-875.
- [4] W. Harrington, S. Braddom, J. Savage, Z. Szoboszlay, R. A. Mckinley, B. Burns, 3D-LZ brownout landing solution, The American Helicopter Society 66th Annual Forum, Phoenix, Arizona, 11-13 May, 2010, pp. 1-19.
[DOI:10.13140/2.1.3831.8725](https://doi.org/10.13140/2.1.3831.8725)
- [5] Z. P. Szoboszlay, B. T. Fujizawa, C. R. Ott, J. C. Savage, S. M. Goodrich, A. Mckinley, J. R. Soukup, 3D-LZ flight test of 2013: landing an EH-60L helicopter in a brownout degraded visual environment, The American Helicopter Society 70th Annual Forum, Montreal, Quebec, 20-22 May, 2014, pp. 2023-2042.

DOI:10.13140/2.1.4978.7525

- [6] Z. Szoboszlay, B. Davis, B. Fujizawa, J. Minor, M. Osmon, Z. Morford, Degraded visual environment mitigation (DVE-M) program, Yuma 2016 flight trials in brownout, The American Helicopter Society 73rd Annual Forum & Technology Display, Fort Worth, Texas, 9-11 May, 2017.
- [7] T. S. Turpin, B. Sykora, G. M. Neiswander, Z. P. Szoboszlay, Brownout landing aid system technology (BLAST), The American Helicopter Society 66th Annual Forum, Phoenix, Arizona, 11-13 May, 2010, pp. 498-515.
- [8] J. D. Keller, G. R. Whitehouse, D. A. Wachspress, M. E. Teske, T. R. Quackenbush, A physics-based model of rotorcraft brownout for flight simulation applications, The American Helicopter Society 62nd Annual Forum, Phoenix, Arizona, 9-11 May, 2006, pp. 1097-1107.
- [9] D. A. Wachspress, G. R. Whitehouse, J. D. Keller, K. Yu, A high fidelity brownout model for real-time flight simulations and trainers, The American Helicopter Society 65th Annual Forum, Grapevine, Texas, 27-29 May, 2009, pp. 1281-1304.
- [10] A. D. Andrea, F. Scorcelletti, Enhanced numerical simulations of helicopter landing maneuvers in brownout conditions, The American Helicopter Society 66th Annual Forum, Phoenix, Arizona, 11-13 May, 2010, pp. 1084-1101.
- [11] G. M. Neiswander, Improving deceleration guidance for rotorcraft brownout landing, The American Helicopter Society 67th Annual Forum, Virginia Beach, Virginia, 3-5 May, 2011, pp. 1010-1031.
- [12] G. R. Whitehouse, D. A. Wachspress, T. R. Quackenbush, J. D. Keller, Exploring aerodynamic methods for mitigating brownout, The American Helicopter Society 65th Annual Forum, Grapevine, Texas, 27-29 May, 2009, pp. 349-364.
- [13] J. K. Tritschler, M. Syal, R. Celi, J. G. Leishman, A methodology for rotorcraft brownout mitigation using rotor design optimization, The American Helicopter Society 66th Annual Forum, Phoenix, Arizona, 11-13 May, 2010, pp. 1674-1690.
- [14] J. Alfred, R. Celi, J. G. Leishman, Flight path optimization for brownout mitigation using a high-fidelity simulation model, *Journal of the American Helicopter Society*, 62 (3) (2017) 1-15.

DOI: <https://doi.org/10.4050/JAHS.62.032012>

- [15] C. C. Ryerson, R. B. Haehnel, G. G. Koenig, M. A. Moulton, Visibility enhancement in rotorwash clouds, 43rd AIAA Aerospace Sciences Meeting and Exhibit, 2005-263.
DOI: [10.2514/6.2005-263](https://doi.org/10.2514/6.2005-263)
- [16] Y. Wenren, J. Walter, M. Fan, J. Steinhoff, Vorticity confinement and advanced rendering to compute and visualize complex flows, 44th AIAA Aerospace Sciences Meeting and Exhibit Reno, 2006.
DOI: <https://doi.org/10.2514/6.2006-945>
- [17] R. B. Haehnel, M. A. Moulton, W. Wenren, J. Steinhoff, A model to simulate rotorcraft-induced brownout, Proceedings of the 64th Annual Forum of the American Helicopter Society, Montreal, Quebec, Canada, 29 April-1 May, 2008, pp. 589-601.
- [18] M. Syal, B. Govindarajan, J. G. Leishman, Mesoscale sediment tracking methodology to analyze brownout cloud developments, Presented at the 66th Annual Forum of the American Helicopter Society, Phoenix, AZ, May 10-13, 2010, pp. 1644-1673.
- [19] S. Thomas, V. K. Lakshminarayan, T. S. Kalra, J. D. Baeder, Eulerian-lagrangian analysis of cloud evolution using CFD coupled with a sediment tracking algorithm, The American Helicopter Society 67th Annual Forum, Virginia Beach, Virginia, May 3-5, 2011, pp. 298-315.
- [20] S. Thomas, M. Amiraus, J. Baeder, GPU-accelerated FVM-RANS hybrid solver for simulating two-phase flow beneath a hovering rotor, The 69th Annual Forum of the American Helicopter Society, Phoenix, AZ, May 24-28, 2013, pp. 2462-2484.
- [21] B. M. Kutz, T. Gunther, A. Rumpf, A. Kuhn, Numerical examination of a model rotor in brownout conditions, Presented at the 70th Annual Forum of the American Helicopter Society, Montreal, Quebec, Canada, May 20-22, 2014, pp. 2450-2461.
- [22] C. Phillips, H. W. Kim, R. E. Brown, The flow physics of helicopter brownout, Present at the American Helicopter Society 66th Annual Forum, Phoenix, AZ, May 11-13, 2010, pp. 1273-1291.
- [23] M. Syal, J. G. Leishman, Predictions of brownout dust clouds compared to photogrammetry measurements, Journal of the American Helicopter Society, 58 (2) (2013) 1-18.
DOI: [10.4050/JAHS.58.022001](https://doi.org/10.4050/JAHS.58.022001)
- [24] B. Govindarajan, J. G. Leishman, Predictions of rotor and rotor/airframe configurational effects on brownout dust clouds, Journal of Aircraft, 53(2) (2015) 545-560.

DOI:10.2514/1.C033447

- [25] C. Pasquali, J. Serafini, G. Bernardini, J. Milluzzo, Numerical-experimental correlation of hovering rotor aerodynamics in ground effect, *Aerospace Science and Technology*, 106 (2020) 106079.

DOI:10.1016/j.ast.2020.106079

- [26] Y. Shao, H. Lu, A simple expression for wind erosion threshold friction velocity, *Journal of Geophysical Research*, 105 (D17) (2000) 22,437-22,443.

<https://doi.org/10.1029/2000JD900304>

- [27] Y. Shao, A. Li, Numerical modeling of saltation in the atmospheric surface layer, *Boundary-Layer Meteorology*, 91 (1999) 199-225.

DOI:10.1023/A:1001816013475

- [28] H. Lu, Y. Shao, A new model for dust emission by saltation bombardment, *Journal of Geophysical Research*, 104 (D14) (1999) 16,827-16,842.

DOI:10.1023/A:1001816013475

- [29] M. Ramasamy, G. K. Yamauchi, Using model-scale tandem-rotor measurements in ground effect to understand full-scale CH-47D outwash, *Journal of the American Helicopter Society*, 62 (1) (2017) 012004-1, 012004-14.

DOI: <https://doi.org/10.4050/JAHS.62.012004>

- [30] J. F. Tan, Y. M. Sun, G. N. Barakos, Vortex approach for downwash and outwash of tandem rotors in ground effect, *Journal of Aircraft*, 55 (6) (2018) 2491-2509.

DOI:10.2514/1.C034740

- [31] M. A. Woodgate, Y. Shi, T. A., Fitzgibbon, G. N. Barakos, P. Li, Simulation of step input in collective pitch for hovering rotor, *Aerospace Science and Technology*, 110 (2021) 106425.

<https://doi.org/10.1016/j.ast.2020.106425>

- [32] J. F. Tan, H. W. Wang, Simulating unsteady aerodynamics of helicopter rotor with panel/viscous vortex particle method, *Aerospace Science and Technology*, 30 (2013) 255-268.

DOI:10.1016/j.ast.2013.08.010

- [33] J. F. Tan, J. G. Cai, G. N. Barakos, C. Wang, Computational study on the aerodynamic interference between tandem rotors and nearby obstacles, *Journal of Aircraft*, 57 (3) (2020) 456-468.

DOI:10.2514/1.C035629

- [34] J. F. Tan, T. Y. Zhou, Y. M. Sun, G. N. Barakos, Numerical investigation of the aerodynamic interaction between a tiltrotor and a tandem rotor during shipboard operations, *Aerospace Science and Technology*, 87 (2019) 62-72.
<https://doi.org/10.1016/j.ast.2019.02.005>
- [35] T. Su, Y. Lu, J. Ma, S. Guan, Aerodynamic characteristics analysis of electrically controlled rotor based on viscous vortex particle method, *Aerospace Science and Technology*, 97 (2020) 105645.
[DOI:10.1016/j.ast.2019.105645](https://doi.org/10.1016/j.ast.2019.105645)
- [36] L. Greengard, V. Rokhlin, A fast algorithm for particle simulations, *Journal of Computational Physics*, 135 (2) (1997) 280-292.
<https://doi.org/10.1006/jcph.1997.5706>
- [37] P. A., Cundall, O. D. L. Strack, A discrete numerical model for granular assemblies, *Geotechnique*, 29 (1979) 47-65.
[DOI:10.1680/geot.1979.29.1.47](https://doi.org/10.1680/geot.1979.29.1.47)
- [38] R. D. Mindlin, H. Deresiewicz, Elastic spheres in contact under varying oblique forces, *Transactions of ASME, Series E. Journal of Applied Mechanics*, 20 (1953) 327–344.
[DOI:10.1007/978-1-4613-8865-4_35](https://doi.org/10.1007/978-1-4613-8865-4_35)
- [39] A. D. Renzo, F. P. D. Maio, Comparison of contact-force models for the simulation of collisions in DEM-based granular flow codes, *Chemical Engineering Science*, 59 (2004) 525-541.
[DOI:10.1016/j.ces.2003.09.037](https://doi.org/10.1016/j.ces.2003.09.037)
- [40] J. S. Light, Tip vortex geometry of a hovering helicopter rotor in ground effect, *Journal of the American Helicopter Society*, 38 (2) (1993) 34-42.
[DOI:10.4050/JAHS.38.34](https://doi.org/10.4050/JAHS.38.34)
- [41] A. Filippone, R. Bakker, P. M. Basset, B. Rodriguez, R. Green, B. Kutz, F. Bensing, A. Visingardi, Rotor wake modelling in ground effect conditions, Presented at the 37th European Rotorcraft Forum, ERF, Vergiate and Gallarate, Italy, 2011, pp. 29-40.
- [42] T. E. Lee, J. G. Leishman, M. Ramasamy, Fluid dynamics of interacting blade tip vortices with a ground plane, *Journal of the American Helicopter Society*, 55 (2) (2010) 22005-1- 22005-16.
[DOI:10.4050/JAHS.55.022005](https://doi.org/10.4050/JAHS.55.022005)

[43] V. K. Lakshminarayan, T. S. Kalra, J. D. Baeder, Detailed computational investigation of a hovering microscale rotor in ground effect, *AIAA Journal*, 51 (4) (2013) 893-909.

[DOI:10.2514/1.J051789](https://doi.org/10.2514/1.J051789)

[44] O. D. Wong, P. E. Tanner, Photogrammetric measurements of an EH-60L brownout cloud, *Journal of the American Helicopter Society*, 61 (1) (2016) 1-10.

[DOI:10.4050/JAHS.61.012003](https://doi.org/10.4050/JAHS.61.012003)

[45] P. E. Tanner, Photogrammetric characterization of a brownout cloud, Presented at the American Helicopter Society 67th Annual Forum, Virginia Beach VA, May 3-5, 2011, pp. 3039-3055.